Article:
Thornton, AR, van der Horn, AJ, Gagarina, E et al. (3 more authors) (2014) Hele-Shaw beach creation by breaking waves: a mathematics-inspired experiment. Environmental Fluid Mechanics, 14 (5). pp. 1123-1145. ISSN 1567-7419

https://doi.org/10.1007/s10652-014-9350-7

Noname manuscript No.
(will be inserted by the editor)

Hele-Shaw Beach Creation by Breaking Waves

A mathematics-inspired experiment

Anthony Thornton · Avraham van der Horn · Elena Gagarina · Wout Zweers · Devaraj van der Meer · Onno Bokhove

Received: date / Accepted: date

Abstract Fundamentals of nonlinear wave-particle interactions are studied experimentally in a Hele-Shaw configuration with wave breaking and a dynamic bed. To design this configuration, we determine, mathematically, the gap width which allows inertial flows to survive the viscous damping due to the side walls. Damped wave sloshing experiments compared with simulations confirm that width-averaged potential-flow models with linear momen-

We acknowledge Gert-Wim Bruggert for technical assistance and dr. Boudewijn de Smeth from the International Institute for Geo-Information Science and Earth Observation in Twente for lending technical equipment. Financial support came from the MultiScale Mechanics and Physics of Fluids groups of Stefan Luding and Detlef Lohse (University of Twente), respectively; the Stichting Free Flow Foundation; and, the Geophysical Fluid Dynamics Program at the Woods Hole Oceanographic Institution, where O.B. did some of the work.

A.R. Thornton
Department of Mechanical Engineering, University of Twente, Enschede, The Netherlands
E-mail: a.r.thornton@utwente.nl

A.J. van der Horn
Department of Physics, University of Twente, Enschede, The Netherlands

E. Gagarina
Department of Applied Mathematics, University of Twente, Enschede, The Netherlands
E-mail: e.gagarina@utwente.nl

D. van der Meer
Department of Physics, University of Twente, Enschede, The Netherlands
E-mail: d.vandermeer@utwente.nl

W. Zweers
FabLab Saxion Hogeschool, Enschede, The Netherlands
E-mail: zweers@dds.nl

O. Bokhove (corresponding author)
School of Mathematics, University of Leeds, LS2 9JT, Leeds, United Kingdom
Department of Applied Mathematics, University of Twente, The Netherlands
E-mail: o.bokhove@leeds.ac.uk

tum damping are adequately capturing the large scale nonlinear wave motion. Subsequently, we show that the four types of wave breaking observed at real-world beaches also emerge on Hele-Shaw laboratory beaches, albeit in idealized forms. Finally, an experimental parameter study is undertaken to quantify the formation of quasi-steady beach morphologies due to nonlinear, breaking waves: berm or dune, beach and bar formation are all classified. Our research reveals that the Hele-Shaw beach configuration allows a wealth of experimental and modelling extensions, including benchmarking of forecast models used in the coastal engineering practice, especially for shingle beaches.

Keywords Hele-Shaw cell · laboratory experiments · mathematical design · shingle beaches · potential flow and shallow water simulations

1 Introduction

1.1 A Slice of Beach

Natural beaches, including those partially enhanced or even completely man-made, are defensive zones that protect large tracts of the world's coastlines against storm surges. This is especially the case in low-lying deltas such as the western and northern parts of The Netherlands, with its combination of a partially and totally reinforced coastline of beaches and dunes, and dikes. The dynamics of the surf zone, concerning the wet zone from the beach to the offshore line where the white capping of wave breaking starts, are very important for understanding how beaches, berms and sand or shingle banks form and erode. Good predictions of surf zone dynamics and the associated particle transport can reveal where suppletion of particulate material will be required to protect the coast, or where dredging is needed to keep navigational channels into harbours open.

Coastal engineers and fluid dynamicists have made great progress in formulating models for waves and currents, and particle transport in and around the surf zone. This progress has provided the fundamentals for operational forecast models such as Telemac, Delft-3D and Xbeach [22]. Current forecast models are founded on decades of research on wave dynamics and beach erosion, especially during storms [27; 20], on the formulation of the sediment and bedload flux transport laws [29; 6; 9; 18], and on direct mathematical analysis [14]. Despite great advances, the fundamental laws of how sand or gravel particles are picked up, transported and deposited by breaking waves remain relatively poorly understood at a fundamental level. This gap in knowledge motivates the goal of the presented work: demonstrating how a novel, compact Hele-Shaw beach configuration and laboratory experiment may shed new light on wave breaking induced particle transport.

The wave breaking process is comprised of complicated two-phase hydrodynamics of water and air, and three-phase flows through its interaction with suspended sediment and the particulate bottom. Due to the reduction of the

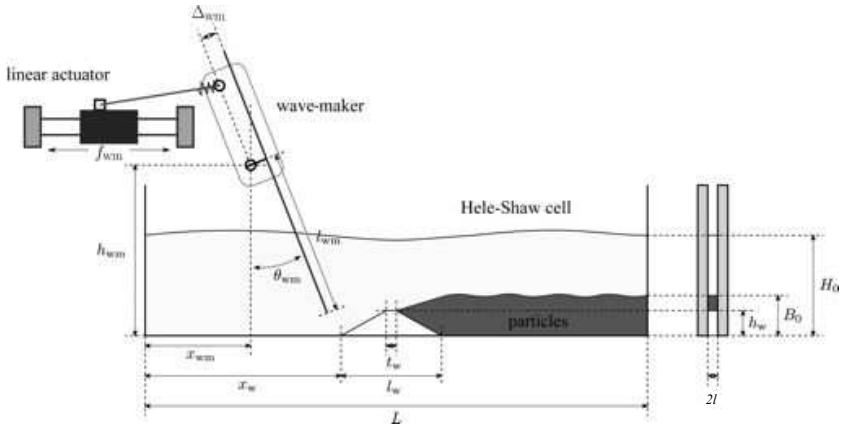

Fig. 1 A schematic front and side view of the Hele-Shaw beach experiment is given. Key parameters varied are the mean free water depth $H_0 - B_0$, initial bed thickness B_0, and wave-maker frequency f_{wm}. Furthermore, $l_{wm} = 333\,\text{mm}$ $l_w = 212\,\text{mm}$, $t_w = 20\,\text{mm}$ and $h_w = 50\,\text{mm}$. The wedge ensures that particles of the bed on the right remain separate from the wave-maker region on the left.

degrees of freedom involved, the focus in the Hele-Shaw beach cell lies on wave-particle interactions while the role of turbulence is greatly reduced. Practically, we investigate the dynamics in a slice of beach: a thin vertical layer of water, air and particle bottom. Hence, the dynamics is made nearly two-dimensional, which effects the reduced role of turbulence as eddies only survice one to two turn-around times. In nature, such a slice of beach would be a few sand or gravel particles thin, tens of meters long and one to a few meters in depth. Instead, this slice of natural beach is scaled down to table-top size, resulting into a Hele-Shaw set-up of about one metre long, a few millimetres wide, and about 30cm in height [4]. Given the relative particle size and the porosity of the bed, this set-up is most closely related to shingle beaches. A sketch of the set-up between two vertical glass plates with closed sides and bottom is provided in Fig. 1. The Hele-Shaw beach is a novel adaptation of the classical set-up by Hele Shaw with single viscous fluid flow around solid obstacles [15; 17]. In contrast to this classical case, the forcing we use is larger and induces inertial flow with wave breaking and limited circulation in the vertical place, cf. inertial flow effects in other work [24; 19; 26]. The dynamics in this modified Hele-Shaw cell takes effectively place in a vertical plane such that gravity is the restoring force permitting surface wave motion. The tank is filled with nearly spherical, zeolite or glass particles and water, and is open at the top. Instead of wind-driven waves or swell travelling onshore, the waves are mechanically driven by a programmable wave-maker. Mostly an inverted swinging pendulum but sometimes also a horizontally moving rod were used as wave-maker. Only minor differences were observed. Next, we present precursory results showing that wave breaking and beach formation are present within the Hele-Shaw beach cell.

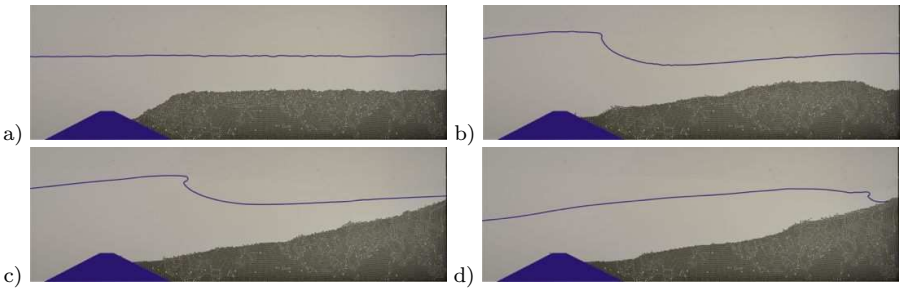

Fig. 2 Beach formation by breaking waves. a) The initial state is shown before the wave-maker (not shown) starts. b) Waves move material from behind the wedge, c) such that over time a beach with nearly constant slope forms on the right (note the spilling breaker). d) The final quasi-steady state has a partially dry beach (note the surging breaker). Particle bed in grey. Waves come from the left. Water line and wedge have been highlighted in blue.

1.2 Precursory Results and Goals

The principal drawback of the Hele-Shaw beach set-up is the proximity of the glass plates because they can lead to heavy damping of the momentum due to a Poiseuille-type lateral flow profile, dominated by viscous effects [15; 17; 24]. To assess these viscous effects, a mathematical analysis was made to enable the design and testing [4; 5]. Hence, the minimal threshold gap width between the glass plates is determined for which a breaking wave or bore can travel to the other end of the tank. The analysis consists of averaging the Navier-Stokes equations for suitable velocity profiles, yielding damped incompressible Euler equations in two dimensions and damped shallow water equations in one spatial dimension. Simulation of this shallow system allows us to calculate an optimal gap width. Using a potential flow Ansatz, we further simplify our damped Euler equations in two dimensions to damped water wave equations. Numerical solutions of these water wave equations have been validated against laboratory experiments of wave sloshing in the Hele-Shaw tank without particles. These address the question:

(i) to what extent is linear momentum damping the primary energy dissipation mechanism in the Hele-Shaw cell?

The primary advantage of the Hele-Shaw beach configuration is that everything becomes clearly visible: the dynamics of each particle and the free surface motion can be traced in time but not at the same time with the set-up used. Although the gap width can be adjusted to become a little over one to a few particle diameters wide, we presently limit ourselves to a gap width of circa 1.1 particle diameter. Particle beds investigated only involve on the order of ten thousand particles.

Wave types classified in the coastal engineering and fluid dynamics literature [3; 23] include spilling, plunging, collapsing and surging breakers. In the literature [3], a distinction of the four wave types above is based on the Iribarren number. Our second goal is therefore to address the question:

(ii) what breaker types do we observe in the Hele-Shaw cell?

The variety of wave breakers observed is intimately related to the evolving bathymetry. While the wave motion favouring bed evolution in the experiment occurs on frequencies of around 1 Hz, bed evolution occurs on longer time scales of minutes to an hour. In Fig. 2, an example of beach evolution is shown. Although the set-up allows for a range of liquid densities, particles sizes, and wave-maker frequencies to be varied, uniformly or non-uniformly, we limit the investigation here to variation of three basic parameters: the monochromatic wave-maker frequency f_{wm}, the still water bed level B_0 and the still water level H_0, for monodispersed nearly spherical particles, see also Fig. 1. The final question we wish to address then becomes:

(iii) what stable quasi-steady beach morphologies are observed in the Hele-Shaw beach as function of these three parameters?

The outline is as follows. In section 2, the mathematical design is presented. The experimental set-up is explained in section 3. Wave sloshing experiments are compared with simulations in section 4. Laboratory results on breaking waves are disseminated in section 5. Quasi-steady beach morphologies are analysed in detail in section 6. Finally, we conclude in section 7.

2 Mathematics of Experimental Design

The main goal of this section is to determine the threshold gap width for which a broken wave can propagate from one end of the tank to the other. Waves generated at one end of the tank usually break when they reach the shallow region behind the wedge. The relevant dimensions concern a tank of a half to one metre in length and with a still water depth H_0 of about 0 to 10 centimetres. We simplify the Navier-Stokes equations of motion for a fixed beach of gentle slope that remains dry onshore. First we scale the equations given the anisotropy of lateral, zonal and depth scales of space and velocity, and average them laterally assuming a Poiseuille-type flow profile across the gap. Subsequently, the resulting planar, incompressible Euler equations are depth-averaged, assuming hydrostatic balance to hold. The threshold gap width is found by using simulations of the resulting shallow water equations for suitable wave forcing.

2.1 Width and Depth Averaging

Our analysis begins with scaling the incompressible Navier-Stokes equations for a homogeneous fluid with velocity field (u^*, v^*, w^*) and pressure p^* as functions of spatial coordinates $(x^*, y^*, z^*)^T$ and time t^*. Partial derivatives are denoted by $\partial_{t^*}(\cdot) = \partial(\cdot)/\partial t^*$, $\partial^2_{y^*}(\cdot) = \partial^2(\cdot)/\partial {y^*}^2$, and so forth. Dimensional coordinates and variables will be denoted with a superscript star. They are

made non-dimensional as follows:

$$u^\star = Uu, \quad v^\star = Vv, \quad w^\star = Ww, \quad x^\star = Lx, \quad y^\star = ly, \quad z^\star = Dz, \tag{1a}$$

$$t^\star = Tt, \quad p^\star = P_0 p, \tag{1b}$$

with zonal, lateral and vectical length and velocity scales L, l, D and U, V, W, respectively. The constant fluid density is $\rho_0 = 998\text{kg/m}^3$, $g = 9.8\text{m/s}^2$ is the Earth's acceleration vector and $\nu = 10^{-6}\text{m}^2/\text{s}$ the kinematic viscosity. The time scale $T \approx L/U \approx l/V \approx D/W$, the pressure scale $P_0 = \rho_0 U^2/(R\,\epsilon^2)$ with a planar friction number $R = Re/\epsilon^2 = UL/\nu$ and the Reynolds number $Re = Vl/\nu$; the Froude number $1/Fr^2 = gD/U^2$, and the aspect ratios $\epsilon = l/L \ll 1$ and $\delta = D/L$,

After scaling, the resulting non-dimensional equations become:

$$\underline{\partial_t u + u\partial_x u + v\partial_y u + w\partial_z u} = \underline{-\frac{1}{R\,\epsilon^2}\partial_x p + \frac{1}{R}\frac{1}{\epsilon^2}\partial_y^2 u} + \frac{1}{R}\big(\partial_x^2 + \frac{1}{\delta^2}\partial_z^2\big)u \tag{2a}$$

$$\partial_t v + u\partial_x v + v\partial_y v + w\partial_z v = -\frac{1}{R\,\epsilon^4}\partial_y p + \frac{1}{R}\frac{1}{\epsilon^2}\partial_y^2 v + \frac{1}{R}\big(\partial_x^2 + \frac{1}{\delta^2}\partial_z^2\big)v \tag{2b}$$

$$\underline{\partial_t w + u\partial_x w + v\partial_y w + w\partial_z w} = \underline{-\frac{1}{R\,\epsilon^2\,\delta^2}\partial_z p - \frac{1}{Fr^2\delta^2}} + \underline{\frac{1}{R}\frac{1}{\epsilon^2}\partial_y^2 w + \frac{1}{R}\big(\partial_x^2 + \frac{1}{\delta^2}\partial_z^2\big)w} \tag{2c}$$

$$\underline{\partial_x u + \partial_y v + \partial_z w} = \underline{0}. \tag{2d}$$

The two tanks used are about 0.6m and 1m long; the typical length scale of the phenomena generated is smaller, about $L = 0.1$m, in part also because the wave-maker is placed at about $1/3^{\text{rd}}$ of the tank's length. Waves are generated with a sinusoidally-driven wave-maker. An upper limit for U is as follows

$$U = 2\pi f_{wm}\theta_{wm} l_{wm} = \mathcal{O}\,(0.1)\,\text{m/s} \tag{3}$$

with wave-maker frequency $f_{wm} \approx 1.3$Hz, wave-maker angle $\theta_{wm} \approx 20^\circ = 1/9\,\text{rad}$ and wave-maker arm $l_{wm} \approx 0.32$m. The friction number $R = 10^3$ to 4×10^4 with $\epsilon^2 = 4\times10^{-4}$ for $U = 0.01$ to 0.1m/s, $L = 0.1$m and $l = 2\times10^{-3}$m. Hence, Reynolds number $Re = 0.5$ to 5. At leading order in ϵ^2, (2) yields $p = p(x, z, t)$ to be y–independent: only the viscous contribution in the y–direction remains of importance in the zonal and vertical momentum equations. Hence, the reduced equations consist of the underlined terms in (2). Next, we assume a balance between pressure gradients and the remaining viscous terms, such that dimensionally

$$u^\star = -\frac{1}{2\rho_0\nu}\partial_{x^\star} p^\star (l^2 - y_\star^2) \quad \text{and} \quad w^\star = -\frac{1}{2\rho_0\nu}(\partial_{z^\star} p^\star + \rho_0 g)\,(l^2 - y_\star^2). \tag{4}$$

A comparison between the magnitude of the inertia terms over the pressure gradient or viscous terms (e.g., [2; 24]), using hydrostatic balance to estimate

the pressure gradient, yields

$$\frac{\rho_0(u_\star^2+w_\star^2)}{L|\nabla_{x^\star z^\star}p^\star|}\frac{16l^4|\nabla_{x^\star z^\star}p^\star|}{\rho_0\nu^2L^2}=\frac{16l^4g\Delta h}{\nu^2L^2}\sim 1 \text{ to } 100. \tag{5}$$

Consequently, inertial terms remain of importance, and there is no global Hele-Shaw flow despite the narrowness of the set-up. This contrasts the purely viscous balance in classical Hele-Shaw flow [15], but is similar to investigations of Hele-Shaw cells with inertial effects, regarding sufficiently strongly, forced Faraday free surface waves [26] or Kelvin-Helmholtz instability [24].

Pohlhausen and others [28; 26; 24] substitute the quadratic approximation

$$u=3\bar{u}(l^2-y^2)/(2\,l^2)\qquad\text{and}\qquad w=3\bar{w}(l^2-y^2)/(2\,l^2) \tag{6}$$

into the underlined part of (2) and then laterally average these equations, using a width average $\bar{u}=\int_{-l}^{l}u(x,y,z,t)\mathrm{d}y/(2l)$, etc. We keep l as a place holder, even though the dimensionless $l=1$. Wilson and Duffy [33] showed this approximation to be rather good in a similar yet different lubrication application, in a comparison with a numerical solution of the Navier-Stokes equations. Ansatz (6) is also a simple numerical discretization of u and w in the y-direction. The width-averaging step is followed by neglecting (Reynolds) stress terms. The resulting system in dimensional form reads

$$\partial_t\bar{u}+\gamma\bar{u}\partial_x\bar{u}+\gamma\bar{w}\partial_z\bar{u}=-\frac{1}{\rho_0}\partial_xP-3\nu\bar{u}/l^2, \tag{7a}$$

$$\partial_t\bar{w}+\gamma\bar{u}\partial_x\bar{w}+\gamma\bar{w}\partial_z\bar{w}=-\frac{1}{\rho_0}\partial_zP-g-3\nu\bar{w}/l^2, \tag{7b}$$

$$\partial_x\bar{u}+\partial_z\bar{w}=0, \tag{7c}$$

with a y–independent pressure $P=P(x,z,t)$ and $\gamma=6/5$ for the quadratic flow profile used. The kinematic free surface and bottom boundary conditions at $z=h(x,t)+b(x,t)$ and $z=b(x,t)$ with water depth $h=h(x,t)$ and bottom height $b=b(x,t)$ are as follows

$$\partial_t(h+b)+\bar{u}\partial_x(h+b)-\bar{w}=0\qquad\text{at}\quad z=h(x,t)+b(x,t), \tag{8a}$$

$$\partial_tb+\bar{u}\partial_xb-\bar{w}=0\qquad\text{at}\quad z=b(x,t). \tag{8b}$$

Hydrostatic balance emerges in the limit $\delta\to 0$ from (2), in non-dimensional terms as $\partial_zp/(Re\,\epsilon^2)+1/Fr^2=0$, or dimensionally as $\partial_{z^\star}P^\star/\rho_0+g=0$. Hence, $P(x,z,t)=\rho_0g\big(h(x,t)+b(x,t)-z\big)$. After depth averaging and neglecting (other Reynolds) stress terms, damped shallow water equations emerge

$$\partial_t(h\bar{\bar{u}})+\partial_x\big(\gamma h\bar{\bar{u}}^2+gh^2/2\big)=-gh\partial_xb+(\gamma-1)\bar{\bar{u}}\partial_x(h\bar{\bar{u}})-3\nu h\bar{\bar{u}}/l^2 \tag{9a}$$

$$\partial_th+\partial_x(h\bar{\bar{u}})=0 \tag{9b}$$

with $h\bar{\bar{u}}(x,t)=\int_b^{h+b}\bar{u}(x,z,t)\mathrm{d}z$. These shallow water equations are augmented with classical hydraulic jump and bore relations to allow for local discontinuities in depth and velocity, for the simpler case with $\gamma=1$. These jump

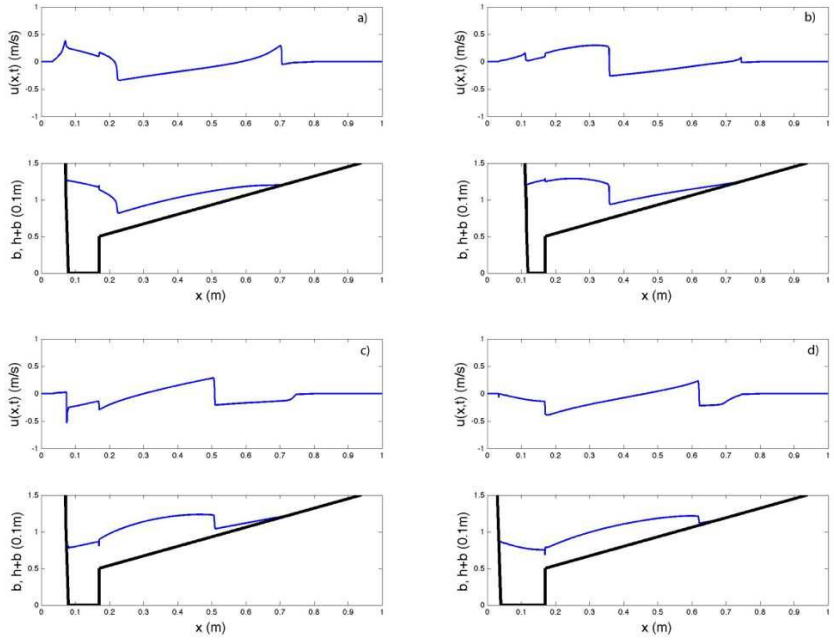

Fig. 3 Our design is based on simulations of shallow-water bore propagation in the Hele-Shaw cell: snapshots of depth-averaged velocity $u(x,t)$, topography $b(x,t)$ (black, fat line) and free surface $h(x,t)+b(x,t)$ (blue, normal line), for a gap width of $2\,l = 2$mm. On the left, a wave-maker is modelled as a steep, moving wall with fixed $\partial_x b(x,t) < 0$, to the right of which the topography $b(x)$ is fixed. a) $t = 3.25T$, b) $t = 3.5T$, c) $t = 3.75T$, and d) $t = 4.0T$ with period $T = 1$s.

relations model breaking waves with energy loss across the bore. Simulations of (9) show that there is a threshold $2\,l \approx 1.5\,$mm for which the bores generated are strong enough to travel across the tank for wave frequencies between 0.5–1Hz. A sample simulation is provided in Fig. 3. For smaller gap widths $2l < 1.5$mm, the bores generated die out too quickly due to the Newtonian momentum damping in the width- and depth-averaged equations (9). Given available and suitable zeolite particles with a diameter of $d = 1.75 \pm 0.05$mm, the gap width in the experimental design was finally chosen as $2l = 2$mm.

3 Experimental Techniques

The primary Hele-Shaw cell consists of two parallel glass plates of length 960mm and a gap of width $2l = 2$mm. It is partially filled with water to a still-water depth of H_0. The wave-maker at one end of the cell consists of a vertical, double welding rod, moving between the glass plates. Each rod has a diameter of 1.6mm. The wave-maker moves approximately back and forth sinusoidally at a fixed amplitude. Three types of experiments are undertaken:

Material	Diameter (mm)	Density (g/cm^3)	Porosity
Gamma Alumina	1.75 ± 0.1	2.08 ± 0.2*	0.53 ± 0.05
Spherical Glass	1.80 ± 0.1	2.515 ± 0.03	0

Table 1 Particle properties. *: Effective density with water-filled pores.

(i) short-time wave sloshing experiments without particles in which the free surface motion is measured, (ii) short-time breaking wave experiments with a movable bed, and (iii) long-time development of quasi-steady beach morphologies with a movable bed of Gamma Alumina particles, see Table 1.

In both the wave sloshing validations and the wave breaking experiments, high speed cameras are used recording images from 500 to 1000 fps. The latter experiments involve about 10^4 particles. In both cases, some red dye is added to the water to increase the contrast between water and air. It has little discernible effect on the surface tension of water. The free-surface locations for arbitrary wave shapes are extracted from the video frames, using codes developed in MATLAB. At the start of a measurement series the set-up is flushed with clean MilliQ® water to which in some cases surfactant was added. The surface tension is therefore not quite the same in all measurements.

For the experiments on beach morphology, photographs are taken every 10s because the time scales involved are longer. The experiments are continued till a quasi-steady beach morphology emerges with little net variation over time. This is assessed visually. An automated analysis is conducted a posteriori to confirm or revoke this visual assessment. Snapshots from a typical measurement were shown in Fig. 2, in which the bed evolved from a flat state to a beach with a nearly constant slope. To analyse such beach formation, a particle tracking code has been developed in MATLAB, determining the location of each particle. The horizontal x-direction is then divided into bins such that the highest (connected) particle in each bin defines the bed profile. To start each experiment a set procedure is followed. Particles are placed into the set-up filled with water a day in advance, such that particle pores saturate with water. The set-up is subsequently flushed with fresh MilliQ® water, resulting in a nearly constant surface tension. The beach is levelled manually and the height B_0 is measured. Subsequently, the set-up is drained and refilled with clean MilliQ® . The range in this fixed room temperature was 23.5 to 28.7°C. The properties of water change only slightly with temperature in this range, and the influence on the results seems negligible. The beach morphology experiments are presented in section 6. Further information can be found in Van der Horn [16].

4 Validating Wave Sloshing Experiments

To assess the validity of the hydrodynamical model (7), we compared numerical water wave solutions based on an exact reduction of (7) *a posteriori* with simple damped wave experiments in our Hele-Shaw cell without particles. We

assume that the domain Ω consists of solid vertical walls at $x = 0$ and L_x, and a fixed flat bottom at $z = 0$ together with a free surface at $z = h(x, t)$. The next step is to impose the velocity field to satisfy $\bar{\boldsymbol{u}} = (\bar{u}, \bar{w}) = \boldsymbol{\nabla}\phi \equiv (\partial_x\phi, \partial_z\phi)$ with velocity potential ϕ in (7). Consequently, the remaining (horizontal) vorticity component $\partial_z\bar{u} - \partial_x\bar{w} = 0$. Combined with the kinematic free surface equation (8a) with $b = 0$, the incompressibility condition yields Laplace's equation with the dynamic and kinematic boundary conditions at $z = h$, i.e.,

$$\partial_t\phi + \frac{1}{2}\gamma|\boldsymbol{\nabla}\phi|^2 + g(h - H_0) + 3\nu\phi/l^2 = 0 \quad \text{at} \quad z = h \tag{10a}$$

$$\partial_t h + (\partial_x\phi)\partial_x h - \partial_z\phi = 0 \quad \text{at} \quad z = h \tag{10b}$$

$$\partial_x^2\phi + \partial_z^2\phi = 0 \quad \text{in} \quad \Omega. \tag{10c}$$

At $x = 0$ and L we have $\partial_x\phi = 0$, and at $z = 0$ we have $\partial_z\phi = 0$. These are classical water wave equations [21] in the vertical plane with additional damping of the velocity potential $\phi_s = \phi(x, z = h, t)$ at $z = h$, cf. [26].

The first and last term in the dynamic boundary condition (10a) can be combined in an integrating factor. For a large damping factor $3\nu/l^2$, potential and kinetic energy will quickly damp out. The extension of Miles' variational principle [21] for water waves based on potential flow then becomes

$$0 = \delta\int_{t_0}^{T}\int_0^L\left(\phi_s\partial_t h - \frac{1}{2}g(h - H_0)^2 - \int_0^{\gamma h}\frac{1}{2}|\boldsymbol{\nabla}\phi|^2\mathrm{d}z\right)\mathrm{d}x e^{3\nu t/l^2}\mathrm{d}t \tag{11}$$

with Neumann conditions at the solid walls and end-point conditions $\delta h(x, t_0) = \delta h(x, T) = 0$. Variation of (11) with respect to ϕ in the interior and the conjugate variables $\{h, \phi_s e^{3\nu t/l^2}\}$ at $z = h$ yields (10). Principle (11) implies that a modified potential energy emerges as

$$P(t)e^{3\nu t/l^2} \equiv \int_0^L \frac{1}{2}\gamma g(h - H_0)^2\mathrm{d}x e^{3\nu t/l^2}, \tag{12}$$

instead of $P(t)$ for stronger damping. Even though the kinetic plus potential energy times $e^{3\nu t/l^2}$ is not conserved, $P(t)e^{3\nu t/l^2}$ oscillates around a positive mean value at later times. Due to the damping, the nonlinear system linearizes at later times, with an energy that is quadratic. Expressed in new variables $\tilde{\phi}_s = \phi_s \exp\left(3\nu t/(2l^2)\right), \tilde{\phi} = \phi \exp\left(3\nu t/(2l^2)\right)$ and $\eta = (h - H_0)\exp\left(3\nu t/(2l^2)\right)$, the variational principle (11) and energy no longer have any explicit time dependence anymore in this long-time limit. A detailed and analogous analysis for the damped nonlinear oscillator that motivated us is found in Gagarina et al. [12].

A straightforward comparison is now made between the potential flow model arising from (10) and an experiment. In the numerical model based on (11) (cf. [10; 11]), we start at rest with a linearly slanted free surface with angle α, see Fig. 4a. Instead, in the experiment we start with a tank at rest lifted upward with an angle α, see Fig. 4b, and lower it down quickly to a horizontal level such as to obtain, approximately, the still profile in Fig. 4a.

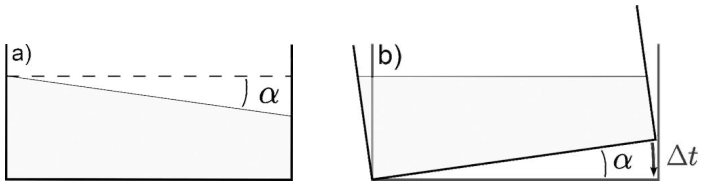

Fig. 4 Initial conditions are shown for a) the simulations starting at rest with a tilted free surface, and b) for the experiments starting at rest with a tilted tank but horizontal free surface.

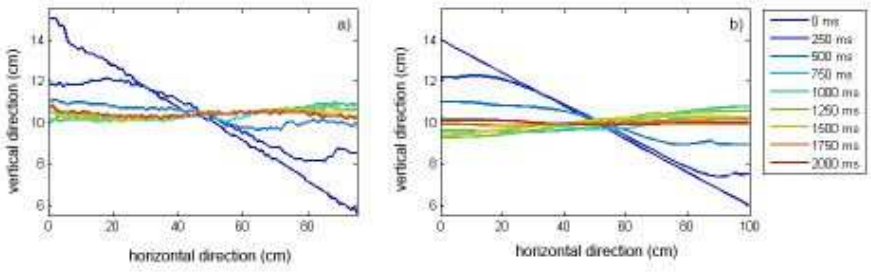

Fig. 5 Free surface profiles in the a) wave sloshing experiment and b) a simulation are shown at different times for a tank or free surface initially titled at $\alpha = 4.6^{\circ}$. Time is rearranged such that the first minimum in $P(t)$ coincides for both experiment and simulation.

Snapshots of the free surface are displayed in Fig. 5 for both a) measurements and b) simulations for times $0, 250, \ldots, 2000$ ms. These compare reasonably well, and in both cases a wave reflects off the right wall around times 250 and 500ms. The small phase difference is removed by shifting the time profiles of $\rho P(t)$ and $\rho P(t) \exp(3\nu t/l^2)$ such that the first zero crossings are lined up. For five values of α, these results are shown in Fig. 6, where we aligned all cases with the first zero crossing at $t = 0$. For the larger angles $\alpha = 6.1^{\circ}$ and $\alpha = 6.5^{\circ}$, our experimental approximation at the start is less satisfactory, but for the other angles the match between the simulations (thin lines) and experiments (thick noisy lines) is good for about one second or period. Within two seconds, most energy has dissipated, but after one second, the comparison with the model is less good, see Fig. 6b. This discrepancy is presumably due to the neglected three-dimensionality of the profile near the free-surface boundary layer in combination with effects of surface tension. In summary, we argue that for the driven flows investigated later, concerning scales much larger than the gap width, linear momentum damping is a good leading-order model approximation because new, long waves keep coming in. The modelling of the fine-structure in breaking waves may require resolution of three-dimensional free-surface boundary layers (cf. [30] in a related yet different free-surface problem on Faraday waves), the inclusion of other flow profiles, and damping of the contact line [31] at the water-air-glass interface. In a Hele-Shaw problem

on Kelvin-Helmholtz instability, Plouraboué and Hinch [24] show that the velocity profiles start to deviate strongly from the parabolic profile for Reynolds numbers of 10 to 30. As inertial effects become more dominant, it is clear that more degrees of freedom in the lateral direction are required.

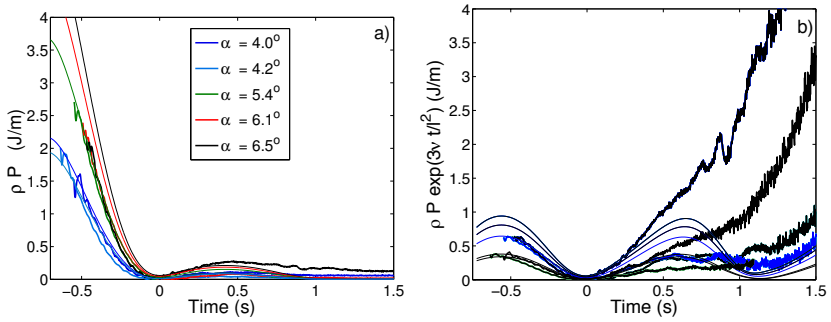

Fig. 6 Potential energies (per unit width) a) $\rho P(t)$, and b) $\rho P(t) \exp(3\nu t/l^2)$, versus time t. Profiles for different initial angles $\alpha = 4.0^{\rm o}, 4.2^{\rm o}, 5.4^{\rm o}, 6.1^{\rm o}, 6.5^{\rm o}$ are shown for the model simulations (thin lines) and the laboratory experiments (thick, jagged lines).

5 Breaking Waves

Four types of breaking waves are described in the literature [13; 23]: spilling, plunging, collapsing and surging breakers, see Table 2. These breaker types can be categorized based on the Iribarren number [3], i.e.,

$$I_b = \tan\alpha / \sqrt{H_b/L_b} = T_w \tan\alpha / \sqrt{2\pi\, H_b/g} \tag{13}$$

with the wave period T_w, slope angle α, and breaker wave height H_b. The wave length $L_b = gT_w^2/(2\pi)$ is based on linear deep water waves, which does seem striking for the shallow water waves considered. At real-world beaches the ordering from spilling, plunging to collapsing to surging breakers is roughly as follows: $I_b < 0.4, 0.4 < I_b < 2.0, 2.0 < I_b < 3.3$, and $I_b > 3.3$, respectively. Qualitatively, this ordering ranges from steep waves on mild slopes for spilling breakers, to shallow waves on steep slopes for surging breakers. The question is how these wave breakers and corresponding Iribarren numbers on real world beaches relate to those observed on Hele-Shaw beaches.

Two series of experiments will be analysed, one in the first 0.6m long Hele-Shaw tank with zeolite particles, and one in the 0.96m tank with glass beads. In both experimental series, all four wave types are to a greater or lesser extent observed, with evidence for the collapsing breaker being the weakest.

In the second series of breaking wave experiments, the experimental procedure is as follows. The values of H_0 and f_{wm} were varied per experiment.

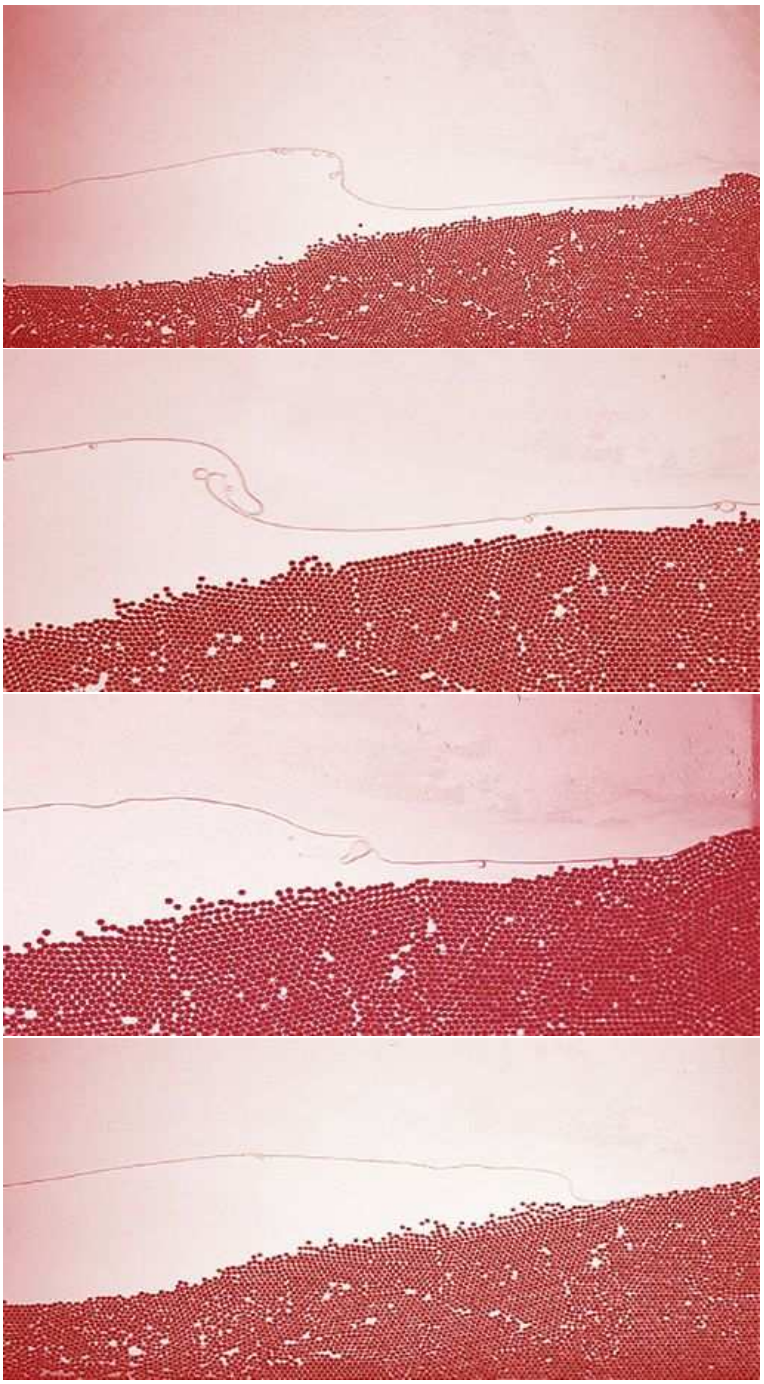

Fig. 7 Top to bottom: still images from spilling, plunging, collapsing and surging breakers (colour enhanced and reversed horizontally for consistency). First series.

Type	Description	Occurrence in cell
Spilling	Bubble-rich water appears at wave crest, spills down front face, sometimes proceeded by projected small jet	In our case bubbles collect at the face, no new bubbles are generated
Plunging	Most of wave's front face overturns and a prominent jet falls near the base of the wave, causing a large splash	Yes
Collapsing	Lower portion of front face overturns and behaves like a truncated breaker	The bottom part of the breaker protrudes, but does not plunge
Surging	No significant disturbance of the smooth wave profile occurs except near the moving shoreline	Yes

Table 2 Definition of the four wave breakers in the real world versus breakers in the Hele-Shaw set-up.

In contrast to the first series, the beach was manually reordered by trial and error into a shape favouring each type of breaker. The phenomenology for each wave breaker will be discussed in the following four paragraphs, see Fig. 7 and Table 2.

Spilling: In the Hele-Shaw cell, the spilling breaker is characterised by pre-existing bubbles accumulating on the crest of the wave. Every cycle, the front face of the wave becomes almost vertical without full breaking. For real-world breakers, white water appears at the wave crest, indicating the presence of many small bubbles, and spills down the front face, sometimes preceded by the projection of a small jet. In contrast, neither bubbles creation is observed at the interface when it is almost vertical, nor the creation of small jets.

Plunging: Snapshots of a plunging breaker are shown in Fig. 8. The wave front overturns (second image) creating a jet near the base of the wave (third image), which leads to a large splash (third and fourth image). The latter splash entrains air that creates a bubble, rising to the surface (sixth image). The dynamics in the set-up is a miniature version of a real-word plunging breaker.

Collapsing: Free surface profiles of a typical collapsing breaker are shown in Fig. 9. This breaker is characterised by splitting of the wave face into an arrested upper part and protruded lower part, which occurs at times 75 to 125ms. We notice that the wave front is almost vertical just before the collapse at around 50ms. The upper part of the wave is seen to move forward, and upward to a certain point, after which its horizontal position remains nearly constant. This may be caused by the two contact lines of the breaker at the glass surfaces. Although the collapsing breaker does show truncation of the practically vertical front face, the lower portion has not been observed to plunge, in contrast to collapsing breakers in the real-world.

Surging: The behaviour of a typical surging breaker observed on the Hele-Shaw beach is shown in Fig. 10. Hardly anything happens till the wave reaches the shore at about 150ms. Then it suddenly overturns and runs up the shore from 150 to 300ms, reaches its highest point, after which point it recedes back (not shown). This surging breaker transports a lot of particulate matter in the

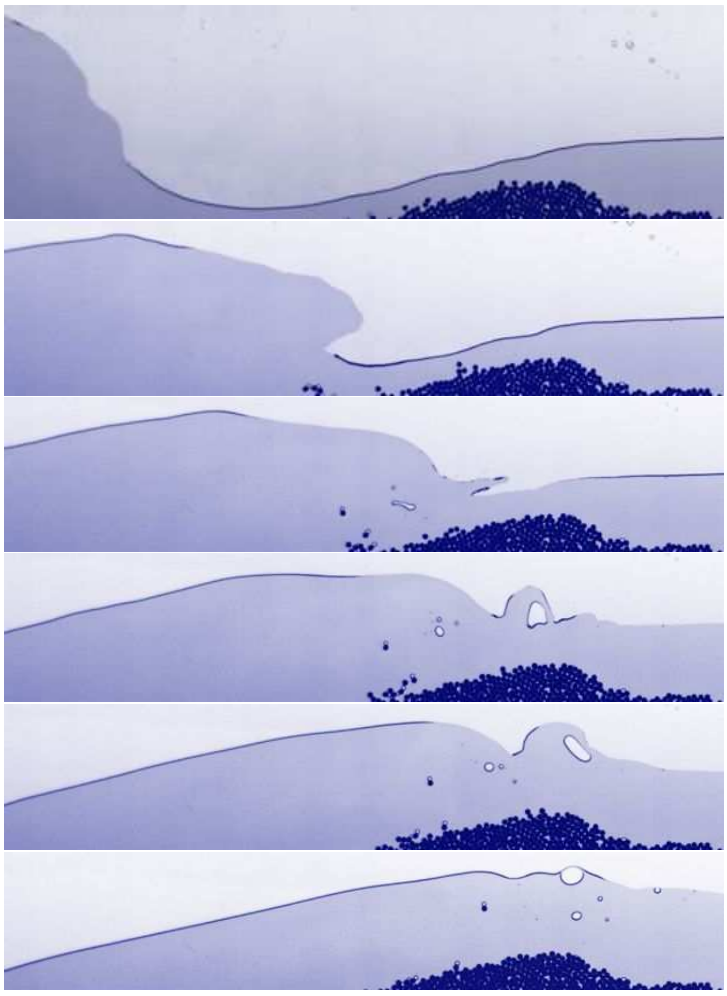

Fig. 8 A sequence of images shows the evolution of a Hele-Shaw plunging breaker (colour enhanced). Top to bottom: $t = 0, 100, 150, 200, 250, 350$ms. Initial water level $H_0 = (98 \pm 1)$mm. Wave-maker frequency $f_{wm} = 1.1$Hz. Second series.

shallow water near the shore. The description of a surging breaker at real-world beaches corresponds well with our observations.

5.1 Iribarren Number

Wave breaking in the first experimental series was filmed with a standard video camera recording at 50fps during various stages of beach formation, using the horizontally moving wave-maker. In contrast to the second series, the bottom slope comprised of the zeolite or Gamma Alumina particles evolved naturally due to the action of the waves. A manual determination using an

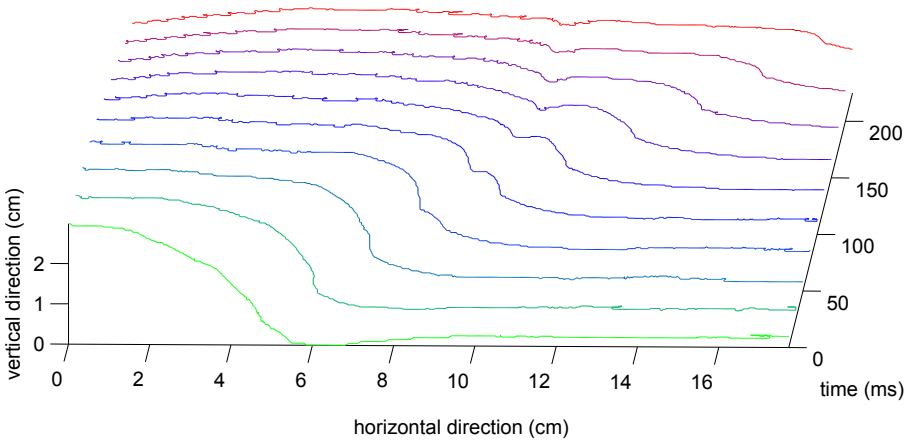

Fig. 9 Free surface profiles for a collapsing breaker. Lines are spaced 25ms apart, denoted in green at early and red at later stages. $f_{wm} = 0.9$Hz. $H_0 = 95 \pm 1$mm.

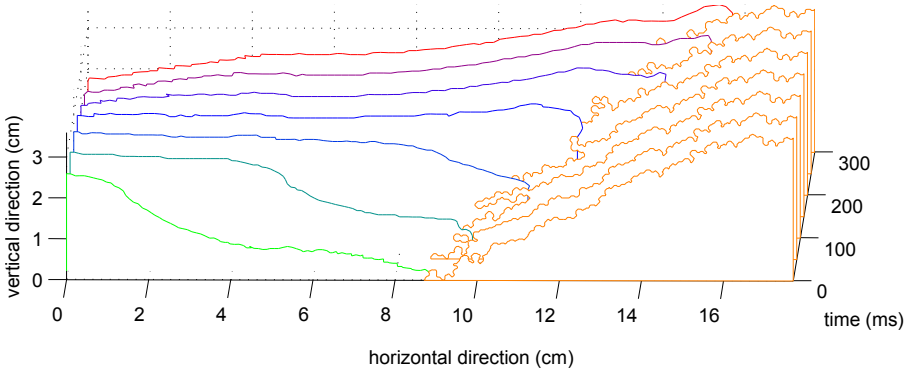

Fig. 10 Waterfall plots are shown for a surging breaker, each 50ms apart. Orange lines indicate the beach location. $H_0 = 95 \pm 1$mm. $f_{wm} = 0.90$Hz. No surfactant is added.

onscreen ruler and protractor of the wave height H (trough to crest) and a mean bottom slope α near wave breaking reveals the following[1]. A definite beach slope is difficult to define clearly in the zone where the wave breaks or starts to break. The corresponding estimated values $\alpha = 22, 27, 29, 26^o$ of the beach slope from surging, collapsing, plunging to spilling breakers, respectively, are therefore prone to contain larger errors. The maximum wave heights $H_b = 4.2, 4.0, 3.8, 6.0$cm estimated are more accurate, as are the wave periods $T = 1.1, 0.8, 0.8$ and 0.8s, respectively. Rough estimates of the resulting Iribarren numbers are $I_b = 1.9, I_b = 1.7, I_b = 1.6$ and $I_b = 0.8$ for surging, collapsing, plunging and spilling breakers.

[1] Source file *golfbakonno2.avi* contains surging, collapsing, plunging and spilling breakers at 8, 133, 115 and 63s, respectively.

All four types of breakers are observed on the Hele-Shaw beach. They lead to a net particle transport and therefore evolution of the bathymetry. The time scale of this evolution is longer, on the order of minutes to an hour, than the time scale of the waves, which are on the order of one half to one-and-a half second. As expected, changes in the bathymetry have a strong effect on the wave dynamics, often leading to a change of breaker type. It is clear from the still photos shown in Fig. 7 that the bathymetry is different for each wave breaker. For the second series, it was not possible to extract the bottom profiles and extract the respective Iribarren numbers, due to the nature the measurements were set up. We observe that: (i) the surging breaker occurs on a beach with two distinct angles; (ii) the collapsing breaker occurs in a beach with a submerged sand-bar (the small elevation under the vertical section of the wave profile); (iii) the plunging breaker is generated over a steep shallow section of the beach, whereas (iv) the spilling breaker rolls over a gently rising bathymetry. Note that these qualifications correspond roughly to to real-world situations, in which surging breakers are often long, low waves over steep bathymetry, while spilling breakers concern steep waves over mildly sloping bathymetry.

Broadly speaking, the plunging breaker transports a great deal of material onto the steep section of the beach; the collapsing breaker moves material from the apex of the submerged sand bar onshore; the spilling breaker is moving material all along the length of the bathymetry; and, finally, the surging breaker is moving material at the break in the bathymetric slope. The trend seems to be that most material is entrained by the wave when the depth is shallow and at locations where there is a change in shape of the bathymetry. The estimated Iribarren numbers are smaller than in nature but their ordering is appropriate.

6 Quasi-Steady Beach Morphologies

Our next step is to demonstrate systematically how beaches and berms in the Hele-Shaw cell are formed by breaking waves. In total 80 measurements were performed to cover the parameter space spanned by wave-maker frequency $f_{wm} \in [0.7, 1.3]$Hz, and the initially quiescent bed and water levels $B_0 \in [5, 8]$cm and $W_0 = H_0 - B_0 \in [1, 8]$cm. All measurements were performed in a semi-random order. This ensured that unforeseen variations of parameters not varied purposely, did not coincide with a gradual variation of the three parameters we did vary systematically. Since adding and removing particles to and from the tank is a slow process, mainly due to the porosity of the Gamma Alumina particles, measurements for each beach height B_0 were performed successively. The results obtained are reproducible for two reasons: the phase diagram presented below shows a coherence that would otherwise be absent, and a total of five measurements was successfully repeated.

Quasi-steady state beach morphologies emerge on a timescale of minutes to an hour. On this timescale, the type of wave motion and wave breaking adjusts

to the changing bed forms. Initially the bed is flat, except near the wedge, and waves may not break. Once the water depth becomes shallower, wave breaking either sets in or becomes more pronounced. In most cases, particles of the bed keep moving during the monochromatic wave cycles, so the beach morphology remains quasi-steady. The experiments are terminated when the state is judged to be quasi-steady and an automated analysis is performed a posteriori.

This analysis, undertaken to establish whether the bed morphology is quasi-steady, is as follows. The difference between the initial state and an evolved state consists of a negative area of moved sediment and a positive area of deposited sediment. These areas differ because the deposited area is more compact by a few percent. An effective distance travelled by the sediment is represented by the distance between the centres of mass of these areas. This distance evolves over time. The bed state is now described by the cubical transport as the product of the (negative) sediment area times the effective distance the sediment travelled. The time derivative thereof yields a cubical transport rate, for which the wave-maker period T_{per} is used as the relevant time unit. Finally, a bed is quasi-steady when this cubical transport rate falls below a threshold of $100\mathrm{mm}^3/\mathrm{T}_{\mathrm{per}}$. That rate corresponds roughly with three bed particles transported over a distance of 1cm per wave-maker period.

An overview of the observed quasi-steady bed morphologies is presented in Fig. 11 and Table 3, with for each morphology the initial quiescent and final quasi-steady state of the bed. Although the transition between these morphologies is smooth, a mathematical classification is based on the minimum and maximum extrema of the (averaged) quasi-steady bed profile $b = b(x)$. A quasi-steady state is deemed (partially) dry if at least one onshore bed particle has dry parts. A swash zone emerges when the bed is alternately immersed and falls dry when the waves run up and down the beach. Due to the interaction with the dynamic bed, some waves are slightly higher than others, even in the quasi-steady phase, such that an extra particle can be swung up the berm or beach. This particle at the top is nearly always (partially) dry if it lies freely at the summit unsupported by the wall. When there is a maximum, it is thus either dry or immersed, in the interior or at the boundary. A berm or dune has a dry interior maximum or island, with water on either side (Fig. 11(a)). A dune-beach has a dry interior maximum with land on the onshore side (Fig. 11b). A submerged bar has a wet interior maximum (Fig. 11(c)). A dry or wet (immersed) beach is a state with a boundary maximum (Fig. 11(d,e)). When nearly no transport occurs because the water is too shallow (or too deep after the wedge), the state is quasi-static (Fig. 11(f)). Finally, in a suction state too many particles disappear over the wedge due to the wave-maker (Fig. 11(g)), with a flat quasi-static part onshore and an interior or boundary minimum near the wedge. This interference inhibits the wave-maker and then the experiment is terminated.

All quasi-steady bed morphologies in the experiment are displayed in Fig. 12 based on the classification outlined above. The evolution of these morphologies is as follows.

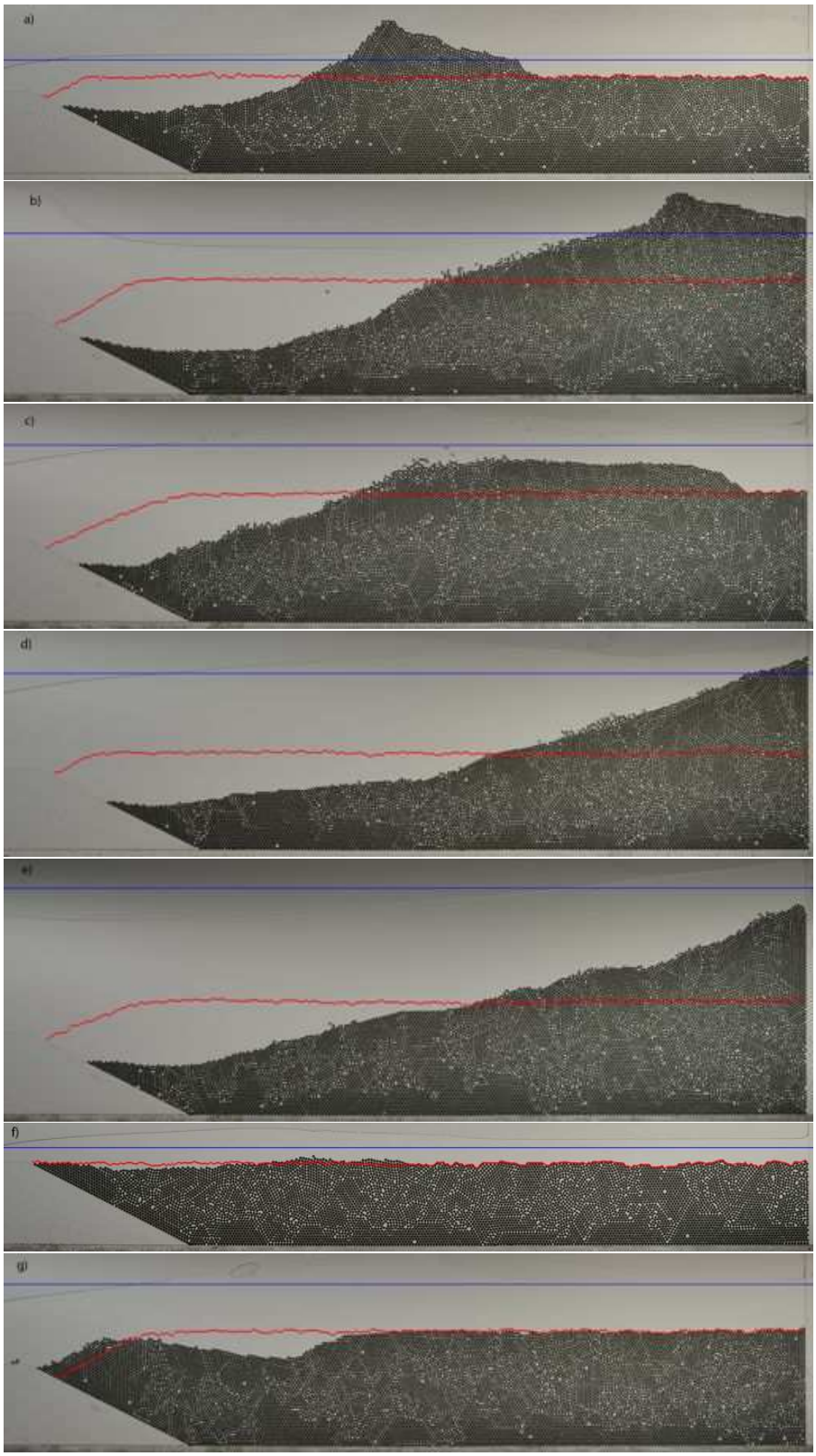

Fig. 11 Quasi-steady bed morphologies and corresponding initial states leading to a classification based on the extrema identified: a minimum or maximum in the interior or the boundary of the bed. Red lines indicate initial bathymetries and blue lines initial water levels. The states are: a) dune/berm and b) dune-beach (dry interior maxima) and c) submerged bar (wet/immersed interior maximum); d) dry and wet beach (boundary maxima); e) quasi-static; and, f) one of suction (interior or boundary minimum with onshore quasi-static part).

SBM	Definition	Quantification
dry beach	beach on onshore side	dry maximum at boundary/wall
immersed beach	beach on onshore side	wet maximum at boundary/wall
dune/berm	island formation	dry interior maximum, water on either side
dune-beach	dry beach with dune	dry interior maximum with dry land beyond
immersed bar	no dry bed parts	wet interior maximum
quasi-static	sediment transport small	wet state
suction	particles sucked to wave-maker	interior/boundary minimum with largely quasi-static bed

Table 3 A classification is given of steady bed morphologies (SBMs) in the Hele-Shaw cell.

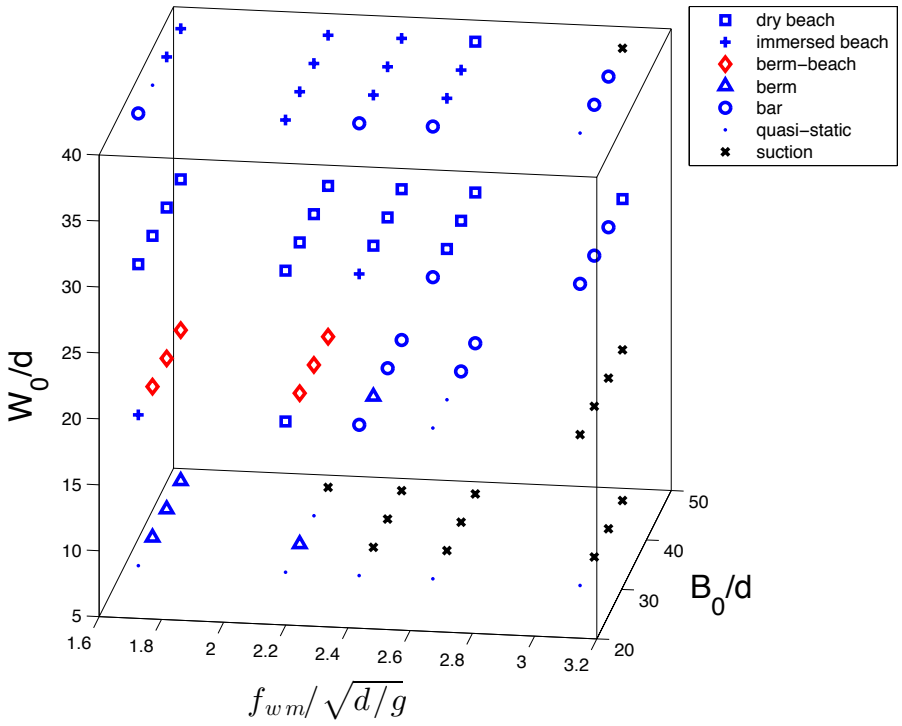

Fig. 12 Phase diagram of all the states as a function of $W_0/d = (H_0 - B_0)/d$, $f_{wm}/\sqrt{d/g}$ and B_0/d.

Typical *berm or dune* formation starts with an initial heap of newly-transported sediment that is formed just behind the wedge (Fig. 13a)). Subsequently, this particle mass starts moving towards the shore and grows, until at some point it breaks through the free surface. Because the water depth is shallow, it induces sufficiently heavy wave breaking, with corresponding dissi-

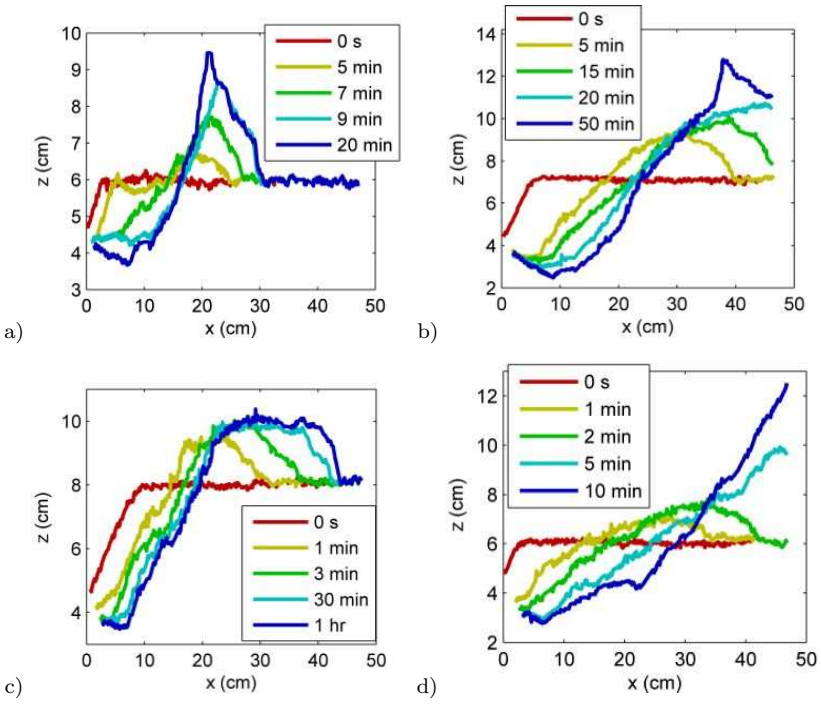

Fig. 13 The formation of a quasi-steady: a) berm or dune $B_0 = 60$mm, $W_0 = 10$mm, $f_{wm} = 0.7$Hz; b) dune-beach $B_0 = 70$mm, $W_0 = 30$mm, $f_{wm} = 0.9$Hz; c) bar $B_0 = 80$mm, $W_0 = 30$mm, $f_{wm} = 1.1$Hz; and, d) beach $B_0 = 60$mm, $W_0 = 50$mm, $f_{wm} = 1.0$Hz.

pation of energy, that further onshore sediment transport is arrested. A berm or dune is formed with wave breaking on its active shore and a calm lake on the other side. Due to the porous structure of the bed, the water level of the lake moves slightly up and down.

Beaches form when the initial water level is deeper (Fig. 13d)). The particle accumulation generated early in the evolution travels to the wall, and keeps growing until a maximum, stable beach angle is reached. Sometimes, the water layer is shallow enough for the beach to emerge from the water, constituting a (partially) dry beach. When the water layer is too deep, the beach stays submerged and wet, because there are insufficient particles available to form a stable dry beach.

A *dune-beach* appears as a transitional form between the beach and dune regions of the parameter space. The bed evolves like the dry beach case, but once it reaches the water surface it switches to a dune-like evolution, giving a rising bed on the onshore side, leading to the formation of a sharp cliff (Fig. 13b).

Suction states are clearly grouped in the part of parameter space where the frequency is high and the water depth is low. During suction, strong offshore

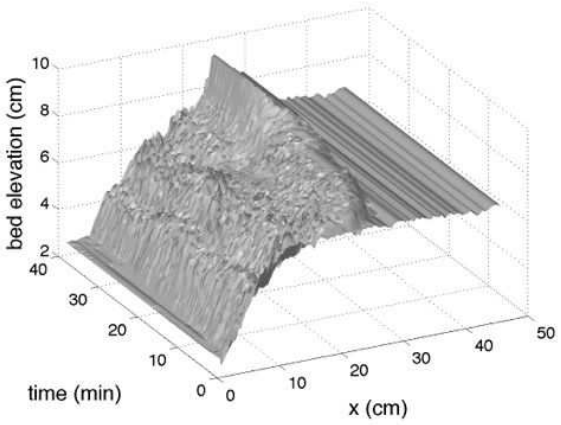

Fig. 14 Dune evolution is displayed as a three-dimensional space-time landscape. $B_0 =$ 60mm.

sediment transport occurs. Hence, the suction part of parameter space is separated from beach and dune states by the quasi-static and bar morphologies.

6.1 Bed Activity and Beach Angles

The free water layer depth, W_0, proves to be the most dominant parameter to determine the type of steady bed morphology. Dunes are observed at shallow water depths $W_0 = 1$cm, beaches at larger depths of about $W_0 = 5$cm, and hybrid dune-beaches at intermediate water layer depths of $W_0 = 3$cm. Bed dynamics is further determined by f_{wm} and B_0. When the initial bed height $B_0 = 5$cm, enough sediment is transported to form beaches in only a few cases, while no dunes or dune-beaches are observed. Suction only occurs in one case. For larger values of B_0, dunes and dune-beaches are formed and more beaches are created, but more instances of suction also occur. Hence, bed activity increases with increasing B_0. We note that the height 5cm of the fixed wedge between wave-maker and bed correlates with the most pronounced jump in bed activity. Concerning the wave-maker frequency, especially the measurements with $B_0 = 5$ and 7 cm suggest a slight optimum in bed transport for $f_{wm} \approx 0.9$Hz. We note that the observed bed morphologies are quite reproducible: the phase diagram in Fig. 12 is coherent. It is clear that beaches, both immersed and dry, are formed when the waves can reach the end of the Hele-Shaw cell without dissipating their wave energy beforehand.

The net particle transport is largest for the berm, beach and bar states. Based on inspection of the wave dynamics, the following is observed. Roughly speaking, two types of particle dynamics can be distinguished, both apparent in the transient phase towards the quasi-steady states and in these states. Rolling and shearing motion of a few layers of particles occurs during wave

motion under a single-valued, gently sloping free surface. Upslope motion appears to lead to more porous dynamic layers than downslope motion. When the free surface is steeper or breaking, particles bounce and saltate in the water column, during vigorous wave breaking occasionally across the entire water column. For surging breakers this happens only near the water line in the swash zone. The net transient or quasi-steady particle transport is a culmination or continuation of this particle dynamics over many wave periods. How do these observations relate to research on granular avalanches in fluids, and especially in Hele-Shaw cells? Courrech du Pont et al. [7] investigate liquid-immersed granular avalanches as function of Stokes number St and grain/fluid density ratio r^2. The Stokes number measures the grain inertia over viscous effects. It is defined as $St = \sqrt{(}\rho_s \Delta\rho g \sin\theta) d^{3/2}/(\nu\rho_0 18\sqrt{2})$ with effective grain density $\rho_s \approx 1500\text{kg/m}^3$ (see Table 1), $\Delta\rho = \rho_s - \rho_0$ and slope θ. Hence, $St \approx 5.0 \pm 0.5$ for three estimates $\theta = 20^o, 25^o, 30^o$ of slopes in our experiment. Cf. [7], the difference between the angle of repose β_r and critical angle β_c is one to two degrees with $\beta_r = 24^o$ for low $St < 10$. Given the results in [7] and the values of $r = \sqrt{\rho_s/\rho_0}$ and St, our system straddles the boundary of the viscous and inertial regimes, in which the particles either reach the Stokes velocity or the inertial velocity, respectively. The Stokes velocity in our Hele-Shaw system is $0.75\Delta\rho g d^2 \sin\theta/(18\nu\rho_0) \approx 0.6\text{m/s}$ with the adjustment factor 0.75 from Lee et al. [19] for the current Hele-Shaw cell of width $1.14d$. (Wall effects are avoided in Courrech du Pont et al. [7] because the tank width is larger than $15d$.) In contrast, Doppler et al. [8] investigate granular avalanches in still fluids and upward water flow in a Hele-Shaw cell of width $\sim 15d$ and $5d$. Their continuum models of the equilibrium flow quite succesfully predict the avalanche dynamics using the shear stress with inertial number, the driving gravity force, side wall friction, and extra fluid forces due to the water flow. Porosity is taken constant at 0.55 and the thickness of the active particle layers is calculated as part of the problem. Such an approach could be a fruitful starting point for modelling the benign phases of the particle dynamics in our experiment under the assumption of slow variations and local equilibirum flow. This approach can, however, probably not capture particle dynamics observed under breaking waves and in the swash zone, and also the observable variations in porosity under smooth wave motion are required. Doppler et al. [8] note that upward flow tends to increase the pile stability while downward water flow tends to decrease it. Albert et al. [1] also consider avalanching of (partially) wet particles with liquid bridges. The slope angles they find are smaller than those observed in the previous two studies, (perhaps due to wall effects) but increase due to cohesive forces caused by liquid bridges. Completely immersed slopes are thus less stable than slopes in the swash zone which are alternatingly immersed and dry. Beach slopes in the swash zone are therefore steeper than the fully immersed slopes of the beach. This difference in stability is used in coastal engineering models [27]. We also observe this in the Hele-Shaw cell: the slope in the dune-beach in Fig. 13b) clearly increases suddenly at the foot of the cliff that appears to mark the start of the swash zone. While this is less

visible in Fig. 13a), a sudden change of slopes between wet beach and cliff is clearly visible for $t > 20$min in another berm case displayed in Fig. 14.

7 Conclusions and Discussion

We presented the mathematical design of a Hele-Shaw cell for the study of bed dynamics by breaking waves. The design shows that damping can be controlled by calculating the gap width of the cell such that driven nonlinear wave motion survives across the tank, while greatly reducing the effects of turbulence and yielding very tractable dynamics.

We showed that all types of real-world wave breakers were also observed on the Hele-Shaw beaches, albeit in idealized forms due to the effects of surface tension. Iribarren numbers were roughly estimated from one of the measurement series, showing the right ordering but other (smaller) values than found on real-world beaches. Finally, a comprehensive parameter study of quasi-steady bed morphologies revealed definite trends in the parameters varied: the levels of the initially flat bed and water at-rest, together with the wave-maker frequency. We could thus identify distinct states at longer times in the bed evolution, such as berms/dunes and beach-dunes, dry and immersed/wet beaches, and bars.

More work is required to relate wave breaking to the bed shape underneath, and to the Iribarren number. Further investigation to assess the role of the wedge (used for technical reasons in the present study), the role of the length and width of the tank, and the role of the wave-maker is also desirable. A more elaborate video capturing system, such that the fast wave motion can (intermittently) be recorded alongside the recording of the natural long-time bed evolution, would be of value.

There are numerous and sensible variations to be made on the laboratory work. These include study of Hele-Shaw beach dynamics under a systematic increase of the gap width to a few particle diameters, and varying the material properties, such as particle properties (size, shape, and density), liquid properties (alcohol-water mixtures), and the effects of glass coatings (to reduce contact line effects).

We presented two preliminary models to enable and assess the mathematical design. Further research is required to extend these models to include the multiphase dynamics observed in the Hele-Shaw cell, in a more or less detailed or averaged manner. The advantage of the Hele-Shaw configuration remains that the quasi-two-dimensional nature of the set-up in principle allows the formulation, study and experimental validation of a hierarchy of models. These can range from the Navier-Stokes equations with explicit particle dynamics for brute-force calculations, to multiphase continuum models and their wave-, width- and depth-averaged versions. Finally, our Hele-Shaw methodology appears useful for benchmarking current wave and sediment forecast models used in coastal engineering [22].

Our beach profiles are remarkably similar to those found in Powell's report [25] for shingle beaches in a $42 \times 1.5 \times 1.4\text{m}^3$ wave tank. The difference is that our mean slope is with circa $1:3$ about two times steeper than the one in Powell [25]. This could possibly be attributed to the greatly diminished long wave reflections caused by the side wall friction. Akin to shingle beaches, beach porosity and porous flow play a visible role in our set-up. We studied the building of berms and beaches from nearly flat ground states. This seems to contrast with (most) larger scale laboratory and numerical studies in which the bed dynamics and total bed transport from the onset lie closer to the equilibrium profiles [32]. A comparison between models and data of Hele-Shaw beach experiments could therefore potentially cover a broader range of bed evolution by breaking waves.

References

1. Albert, R., Albert I., Hornbaker, D., Schiffer P., Barabási, A.-L. 1997: Maximum angle of stability in wet and dry spherical granular media. *Physical Review E* **56**, 6271–6274.
2. Batchelor, G.K. 1967: *An Introduction to Fluid Dynamics.* Cambridge University Press. 635 pp.
3. Battjes, J. 1974: Surf similarity. Proc. 14$^{\text{th}}$ Coastal Eng. Conf., Copenhagen, Denmark, 466–480
4. Bokhove, O., Zwart, V., Haveman, M.J., 2010: *Fluid Fascinations.* Publication of Stichting Qua Art Qua Science, University of Twente. The Hele-Shaw beach was revealed at the Qua Art Qua Science lecture by O.B. and W.Z. on 17-01-2010, in a tribute to the late Prof. Peregrine. http://eprints.eemcs.utwente.nl/17393/
5. Bokhove, O., Van der Horn, A., Van der Meer, D., Zweers, W, Thornton, A.R. 2012: Breaking waves on a dynamic Hele-Shaw beach. Proc. Third Int. Symposium on Shallow Flows. http://eprints.eemcs.utwente.nl/21539/
6. Calantoni, J. Puleo, J.A., Holland, K.T. 2006: Simulation of sediment motions using a discrete particle model in the inner surf and swash-zones. *Cont. Shelf Res. 26*, 1987–2001
7. Courrech du Pont, S., Gondret, P., Perrin, B., Rabaud, M. 2003: Granular avalanches in fluids. *Phys. Rev. Lett.* **90**, 044301-1.
8. Doppler, D., Gondret, P., Loiseleux, T, Meyer, S., Rabaud, M. 2007: Relaxation dynamics of water-immersed granular avalanches. *J. Fluid Mech.* **577**, 161–181.
9. Garnier, R., Dodd, N., Falquez, A., Calvete, D. 2010: Mechanisms controlling crescentic bar amplitude. *J. Geophys. Res.* **115**, F02007
10. Gagarina, E., Van der Vegt, J.J.W., Ambati, V.R., Bokhove O. 2012: A Hamiltonian Boussinesq model with horizontally sheared currents. Third Int. Symp. on Shallow Flows Proc. June 4-6, Iowa, http://eprints.eemcs.utwente.nl/21540

11. Gagarina, E., Ambati, V.R., Van der Vegt, J.J.W., Bokhove, O. 2013: Variational space-time (dis)continuous Galerkin finite element method for nonlinear water waves. Accepted with minor corrections *J. Comp. Phys.*
12. Gagarina, E., Ambati, V.R, Van der Vegt, J.J.W., Nurijanyan, S., Bokhove, O. 2013: Variational time (dis)continuous Galerkin finite element method for nonlinear Hamiltonian systems. In preparation.
13. Galvin, C.J. 1968: Breaker type classification on three laboratory beaches. *J. Geophys. Res.* **73**, 3651–3659
14. Grimshaw, R., Osaisai, E. 2013: Modelling the effect of bottom sediment on beach profiles and wave set-up. *Ocean Modelling* **59–60**, 24–30.
15. Hele-Shaw, H.S. 1898: The flow of water. *Nature* **58**. 520–520.
16. Horn, van der, A.J. 2012: Beach Evolution and Wave Dynamics in a Hele-Shaw Geometry. M.Sc. Thesis, Department of Physics, University of Twente
17. Lamb, H. 1993: *Hydrodynamics.* Cambridge University Press.
18. Lane, E.M., Restrepo, J.M. 2007: Shoreface-connected ridges under the action of waves and currents. *J. Fluid Mech.* **582**, 23–52
19. Lee, A.T., Ramos, E., Swinney, H.L. 2007: Sedimenting sphere in a variable-gap Hele-Shaw cell. *J. Fluid Mech.* **586**, 449–464
20. McCall, R.T., van Thiel de Vries, J.S.M., Plant, N.G., van Dongeren, A.R., Roelvink, J.A., Thompson, D.M., Reniers, A.J.H.M. 2010: Two-dimensional time dependent hurricane overwash and erosion modeling at Rosa Island. *Coastal. Eng.* **57**, 668–683
21. Miles, J. 1977: On Hamilton's principle for surface waves. *J. Fluid Mech.* **83**, 153–158
22. Operational forecasting models 2013: Delft3D. Software platform including morphology of Deltares, The Netherlands: http://www.deltaressystems.com/hydro/product/621497/delft3d-suite
Open Telemac-Mascaret: http://www.opentelemac.org/
XBeach: http://oss.deltares.nl/web/xbeach/
23. Peregrine, D.H. 1983: Breaking waves on beaches. *Ann. Rev. Fluid Mech.* **15**, 149–178
24. Plouraboué, F., Hinch, E.J.. 2002: Kelvin-Helmholtz instability on a Hele-Shaw cell. *Phys. Fluids 14*, 922-929.
25. Powell, K.A. 1990: Predicting short term profile response for shingle beaches. HR Wallingford. Online Report.
26. Rajchenbach, J., Lerouz, A., Clamond, D. 2011: New standing solitary waves. *Phys. Rev. Lett.* **107**, 024502.
27. Roelvink, D., Reniers, A., van Dongeren, A., van Thiel de Vries, J., McCall, R., Lescinkski, J. 2009: Modelling storm impacts on beaches, dunes and barrier islands. *Coastal Eng.* **56**, 1133–1152
28. Rosenhead, L. (ed.) 1963: *Boundary layer theory.* University Press Oxford. 688 pp.
29. Soulsby, R. 1997: *Dynamics of Marine Sands.* In: HR Wallingford. Thomas Telford. 249 pp.
30. Vega, J.M., Knobloch E., and Martel, C. 2001: Nearly inviscid Faraday waves in annular containers of moderately large aspect ratio. *Physica D*

154, 313–336.
31. Vella, D. and Mahadevan, L. 2005: The 'Cheerios Effect'. *American J. Physics* **73**, 817–825.
32. Williams, J., Ruiz de Alegria-Arzaburu, A., McCall R.T., Van Dongeren A., 2012: Modelling gravel barrier profile response to combined waves and tides using XBeach: Laboratory and fields results. *Coastal Engineering* **63**, 62–80.
33. Wilson, S.K., Duffy, B.R. 1998: On lubrication with comparable viscous and inertia forces. *Q.J. Mech. Appl. Math.* **51**, 105–124.